

# Nonlinear hydrodynamic phenomena in Stokes flow regime

**R. H. Goodman<sup>1</sup>, Y.-N. Young<sup>1</sup>, N. Khurana<sup>2</sup>, J. Bławdziewicz<sup>2</sup> and E. Wajnryb**

<sup>(1)</sup> Department of Mathematical Sciences and Center for Applied Mathematics and Statistics, NJIT, Newark, NJ, 07102, USA

<sup>(2)</sup> Department of Mechanical Engineering, Yale University, P. O. Box 208286, New Haven, CT 06520-8286, USA

<sup>(3)</sup> Institute of Fundamental Technological Research, Swietokrzyska 21, 00-049 Warsaw, Poland

CAMS Report 0809-16, Spring 2009

**Center for Applied Mathematics and Statistics**

**NJIT**

# Nonlinear hydrodynamic phenomena in Stokes flow regime

R. H. Goodman<sup>a</sup>, Y.-N. Young<sup>a</sup>, N. Khurana<sup>b</sup>, J. Bławdziewicz<sup>b</sup>, E. Wajnryb<sup>c</sup>

<sup>a</sup>*Department of Mathematical Sciences, New Jersey Institute of Technology, Newark, NJ 07102-1982*

<sup>b</sup>*Department of Mechanical Engineering, Yale University, P.O. Box 208286, New Haven, CT 06520-8286*

<sup>c</sup>*Institute of Fundamental Technological Research, Świętokrzyska 21, 00-049 Warsaw, Poland*

---

## Abstract

We investigate nonlinear phenomena in dispersed two-phase systems under creeping-flow conditions. We consider nonlinear evolution of a single deformed drop and collective dynamics of arrays of hydrodynamically coupled particles. To explore physical mechanisms of system instabilities, chaotic drop evolution, and structural transitions in particle arrays we use simple models, such as small deformation equations and effective medium theory. We find numerical and analytical solutions of the simplified governing equations. The small-deformation equations for drop dynamics are analyzed using results of dynamical-systems theory. Our investigations shed new light on the dynamics of complex fluids, where the nonlinearity often stems from the evolving boundary conditions in Stokes flow.

---

## 1. Introduction

The Navier–Stokes equations contain the inertial term that gives rise to numerous nonlinear phenomena, such as flow instabilities [1], complex convective patterns [2], and turbulence [3]. However, there also exist nonlinear hydrodynamic phenomena that are not due to nonlinear inertial contributions. These nonlinear phenomena occur under creeping-flow conditions in interfacial and particulate flows. The Stokes equations governing the fluid flow are linear so the nonlinearity stems entirely from the evolving boundary conditions.

We present two examples of multiphase systems that exhibit complex nonlinear behavior under creeping-flow conditions. The first system is a deformable highly viscous drop in a two-dimensional (2D) linear flow. The second example is an ordered array of rigid spherical particles in strongly confined Poiseuille flow. The nonlinear coupling in the first system results from the influence of the external flow on the shape of the deformed drop. The nonlinearity in the other system stems from the hydrodynamic interactions between particles.

The interplay between the flow and moving phase boundaries produces diverse nonlinear effects in the two systems under discussion. For viscous drops, there occurs a hysteretic response of the drop shape to quasistatic change of the external flow vorticity, and we also observe period-doubling bifurcations leading to chaos, for periodically varying vorticity [4]. In the other system the interaction between regular particle arrays and Poiseuille flow results in propagation of particle-displacement waves, sudden lattice rearrangements, order-disorder transitions, and fingering instabilities [5]. We elucidate the underlying physical mechanisms of these phenomena.

Our paper is organized as follows: In Sec. 2 we discuss the dynamics of viscous drops in 2D linear flows with rotation. In Sec. 3 we analyze collective dynamics of ordered particle arrays in Poiseuille flow in a parallel-wall channel. Our conclusions are presented in Sec. 4.

## 2. Hysteretic and chaotic drop dynamics

The evolution of a deformable viscous drop is considered in linear creeping flows with rotation. We focus on systems where the drop viscosity is much higher than the continuum phase viscosity. In the creeping-flow regime, the evolving boundary conditions due to the motion of drop interface are the only source of nonlinear dynamics.

We find that nonlinear coupling of the drop deformation and rotation to the external flow results in drop bistability and hysteresis in quasistatic drop-shape evolution. We also analyze a novel chaotic drop dynamics resulting from a period-doubling bifurcation cascade.

### 2.1. Viscous drop in creeping flows

We consider a viscous drop immersed in an incompressible fluid of a constant viscosity  $\mu$ . The viscosity of the drop is  $\hat{\mu} = \lambda\mu$  (where  $\lambda$  is the viscosity ratio), and the interfacial tension between the two phases is  $\sigma$ . The fluid velocity  $\mathbf{u}$  and pressure  $p$  in the regions inside and outside the drop are described by the Stokes equations

$$\mu_i \nabla^2 \mathbf{u} = \nabla p, \quad (1)$$

$$\nabla \cdot \mathbf{u} = 0, \quad (2)$$

where  $\mu_i = \hat{\mu}$  or  $\mu$  is the corresponding fluid viscosity. The nonlinear boundary condition on the drop interface is the balance of normal stress with the capillary pressure

$$[\hat{\mathbf{n}} \cdot \boldsymbol{\tau} \cdot \hat{\mathbf{n}}] = 2\kappa\sigma, \quad (3)$$

where  $\boldsymbol{\tau}$  is the viscous stress tensor,  $\hat{\mathbf{n}}$  is the outward normal unit vector, and  $\kappa$  is the local curvature of the interface.

The drop is subject to a two-dimensional linear incident flow

$$\mathbf{u}_0(\mathbf{r}) = \dot{\gamma}(\mathbf{E}_s + \beta\boldsymbol{\Omega}) \cdot \mathbf{r}, \quad (4)$$

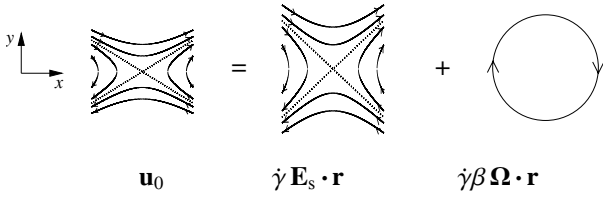


Figure 1: Decomposition of a linear incident flow into pure strain and rigid-body rotation.

where  $\dot{\gamma}$  is the strain rate,  $\beta$  is the dimensionless vorticity parameter,  $\mathbf{r}$  is the position, and

$$\mathbf{E}_s = \frac{1}{2} \begin{pmatrix} 0 & 1 & 0 \\ 1 & 0 & 0 \\ 0 & 0 & 0 \end{pmatrix}, \quad \mathbf{\Omega} = \frac{1}{2} \begin{pmatrix} 0 & 1 & 0 \\ -1 & 0 & 0 \\ 0 & 0 & 0 \end{pmatrix} \quad (5)$$

are the symmetric and antisymmetric parts of the velocity-gradient tensor. The symmetric part describes a purely straining flow, and the antisymmetric part corresponds to rigid-body rotation with the angular velocity  $\omega = \frac{1}{2}\beta\dot{\gamma}$ . The decomposition of incident flow (4) into the straining and vorticity components associated with tensors  $\mathbf{E}_s$  and  $\mathbf{\Omega}$  is sketched in Fig. 1.

Three dimensionless parameters characterize the dynamics of the viscous drop. The viscosity ratio  $\lambda$  describes the rel-

ative magnitude of dissipative forces in the drop-phase and continuous-phase fluids. The capillary number  $Ca = a\mu\dot{\gamma}/\sigma$  (where  $a$  is the radius of an undeformed drop) gives the ratio between the deforming viscous forces produced by the imposed flow (4) and the capillary forces driving the drop towards the equilibrium spherical shape. Finally, the vorticity parameter  $\beta$  describes the magnitude of the rotational component of the external flow relative to the extensional component.

## 2.2. Bistable stationary states and hysteresis

For sufficiently large viscosity ratios ( $\lambda > 100$ ) and moderate capillary numbers (below the critical value for drop-breakup instability), two stable stationary drop shapes are found for a range of  $\beta$  between critical values  $\beta_1$  and  $\beta_2$ . These two stationary states are illustrated in Fig. 2. The drop shape shown in Fig. 2(a) is elongated and nearly aligned with the extensional axis  $x = y$ ; the shape shown in Fig. 2(b) is nearly spherical [6].

The elongated stationary shape results from the balance between drop deformation by the extensional flow component and drop relaxation due to the capillary forces. The respective time scales for the drop deformation and relaxation are  $t_\gamma = \lambda\dot{\gamma}^{-1}$  and  $t_\sigma = \lambda\mu a\sigma^{-1}$ , both of which are proportional to the viscosity ratio for  $\lambda \gg 1$ . The drop deformation  $D = (l-2a)/a$  (where  $l$  denotes the drop length) is determined by the time scale ratio

$$D \sim t_\sigma/t_\gamma = Ca. \quad (6)$$

Therefore,  $D$  is independent of the viscosity ratio in the limit  $\lambda \rightarrow \infty$ . The  $O(\lambda^{-1})$  internal circulation inside an elongated high-viscosity drop is weak for large  $\lambda$ . Thus the drop behaves like a rigid body whose equilibrium orientation results from the balance of the torques produced by the straining and rotational components of the external flow, as depicted in Fig. 2(a).

The compact stationary shape is stabilized by the circulation of the fluid inside the drop, which rotates with an angular velocity  $\omega_d$ , nearly equal to the angular velocity  $\omega$  of the external flow. Within each period of rotation the drop undergoes a small deformation produced by the straining component of the external flow, as schematically illustrated in figure 2(b). However, the deformation does not grow, because it is constantly convected away by the rotational component of the flow. Since the rotation occurs on the time scale  $t_{\text{rot}} = (\beta\dot{\gamma})^{-1}$ , and the drop deforms on the much longer timescale  $t_\gamma = \lambda\dot{\gamma}^{-1}$ , we find that the drop deformation in the compact state,

$$D \sim t_{\text{rot}}/t_\gamma = (\beta\lambda)^{-1}, \quad (7)$$

is small for  $\lambda \gg 1$ .

The existence of two stationary states implies a hysteretic drop response to quasistatic variation of vorticity  $\beta$ . Such hysteresis in the drop length  $l$  is depicted in Fig. 2(c). The results are from direct numerical simulations using the boundary-integral method [7].

For  $\beta$  in the range between  $\beta_1$  and  $\beta_2$  (the two critical values labeled in 2(c)), the drop assumes either an elongated or compact shape, which correspond to two stationary values of the drop length. When the maximal torque  $\tau_\gamma$  exerted on the drop

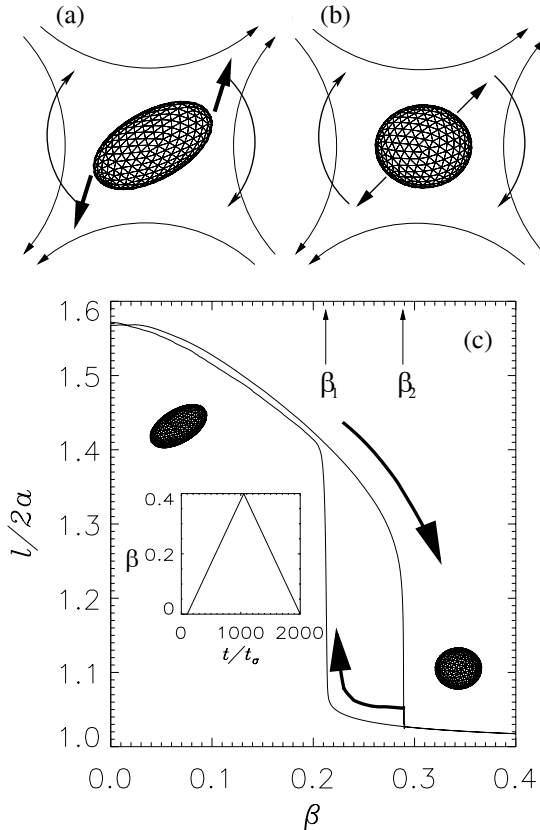


Figure 2: (a) Surface-tension-stabilized elongated drop. (b) Rotationally stabilized compact drop. (c) Hysteresis of a highly viscous drop in 2D linear flow with varying vorticity. Results are from boundary-integral simulations with  $\lambda = 200$  and  $Ca = 0.20$ . Inset shows the dependence of vorticity on time.

by the straining flow component marginally balances the torque  $\tau_{\text{rot}}$  resulting from the vorticity flow component, there occur transitions between the elongated and compact drop shapes. Since the straining component produces a non-zero torque only on elongated shapes, and  $\tau_{\text{rot}}$  is approximately independent of  $D$ , we obtain the scaling relations

$$\tau_\gamma \sim D, \quad \tau_{\text{rot}} \sim \beta. \quad (8)$$

Assuming torque balance  $\tau_\gamma \approx \tau_{\text{rot}}$  near a transition point and combining relations (8) with the estimates (7) and (6) for the drop deformation in the compact and elongated states, we find the scaling relations

$$\beta_1 \sim \lambda^{-1/2}, \quad (9)$$

$$\beta_2 \sim \text{Ca} \quad (10)$$

for the lower and upper critical vorticity parameters. These scaling relations can also be derived from the small deformation equations discussed in Sec. 2.3.2.

### 2.3. Period-doubling bifurcations and chaotic drop dynamics

The existence of bistable stationary states of a dynamical system often leads to interesting nonlinear response to periodic forcing. We examine drop evolution in straining flow with periodic vorticity variation

$$\beta(t) = \bar{\beta} + \delta\beta \sin(2\pi t/T), \quad (11)$$

where  $\bar{\beta}$  is the average vorticity,  $\delta\beta$  is the vorticity-oscillation amplitude,  $T$  is the oscillation period, and  $t$  is time. We show that despite the laminar nature of Stokes flow, the drop evolution is chaotic for some parameter values. We present numerical examples (Sec. 2.3.1), an analytical description using asymptotic small-deformation equations (Sec. 2.3.2), and dynamical-systems analysis (Secs. 2.3.3 and 2.3.4).

#### 2.3.1. Drop response to harmonic vorticity variation

Figure 3 shows our boundary-integral simulations for drop-length evolution in a system with periodic vorticity variation (11). The mean value of the vorticity,  $\bar{\beta} = 0.21$ , is near the lower critical value (9), and the oscillation amplitude  $\delta\beta = 0.13$  spans the range of the hysteresis loop.

The results indicate that for short periods  $T$  of vorticity variation (compared with the drop relaxation time  $t_\sigma$ ) the drop undergoes regular oscillations around the compact stationary shape, as shown in Fig. 3(a). Drop evolution is also periodic at large values of  $T$ : for  $T \approx 4t_\sigma$  drop oscillates around the elongated stationary shape (Fig. 3(d)), and for  $T \gg t_\sigma$  quasistatic evolution is obtained (Fig. 3(e)).

For intermediate values of the oscillation period  $T \approx t_\sigma$  the drop response to periodic forcing is irregular, which is seen in Figs. 3(b) and 3(c). Using small-deformation equations we argue that this irregular response is associated with transition to chaos.

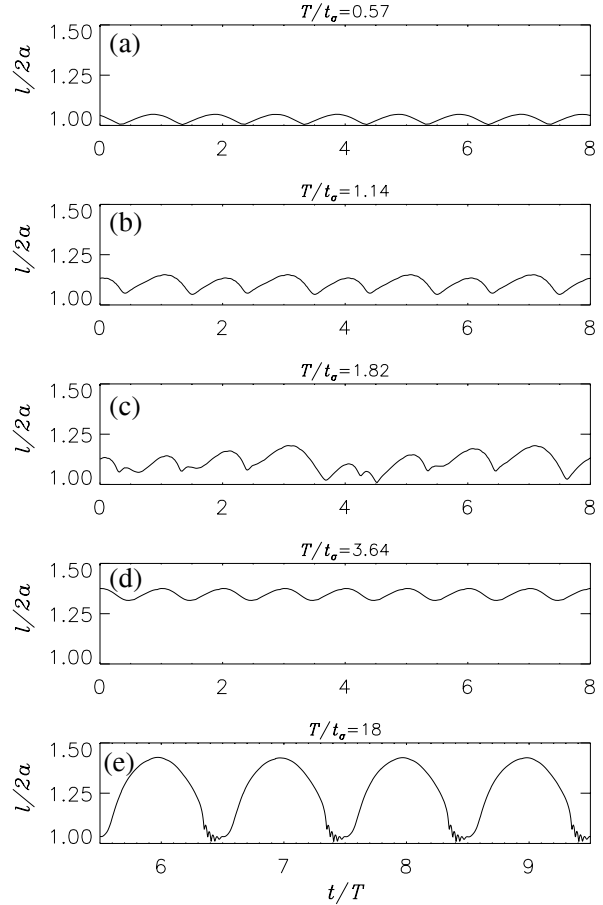


Figure 3: Evolution of drop length in planar linear flow with harmonic variation of vorticity for different values of period  $T$  normalized by drop-relaxation time (as labeled). Mean vorticity  $\bar{\beta} = 0.21$ , vorticity amplitude  $\delta\beta = 0.13$ , viscosity ratio  $\lambda = 275$ , and capillary number  $\text{Ca} = 0.2$ . Panel (c) depicts chaotic dynamics. (Results from boundary-integral simulations.)

#### 2.3.2. Small-deformation equations

In our further analysis we use small-deformation equations based on the expansion of the drop shape into spherical harmonics [8]. Near the bifurcation that leads to shape hysteresis, the drop evolution can be described by asymptotic small-deformation equations in which only two modes are retained.

Accordingly, the position of the drop interface  $r_s$  is expanded into the second-order spherical harmonics,

$$r_s/a = 1 + \sqrt{2}[f \text{Re}Y_{22}(\Omega) + g \text{Im}Y_{22}(\Omega)], \quad (12)$$

where  $\Omega = (\theta, \phi)$  is the solid angle and  $f$  and  $g$  are the drop-shape perturbation amplitudes. Since  $\text{Re}Y_{22} \sim \cos 2\phi$  and  $\text{Im}Y_{22} \sim \sin 2\phi$  (where  $\phi$  is measured from the axis  $x$ ), the amplitude  $f$  describes drop deformation along the symmetry axis  $x$ , and the amplitude  $g$  corresponds to the deformation along the straining axis  $x = y$ .

As shown in [6], the asymptotic small-deformation equations

for the shape amplitudes  $f$  and  $g$  have the form

$$\frac{df}{dt} = -2\omega_d g - \lambda^{-1} \text{Ca}^{-1} D_0 f, \quad (13a)$$

$$\frac{dg}{dt} = 2\omega_d f - \lambda^{-1} \text{Ca}^{-1} D_0 g + \lambda^{-1} d_0. \quad (13b)$$

Here  $D_0 = 20/19$  and  $d_0 = (5\pi/6)^{1/2}$  are numerical coefficients, and

$$\omega_d = -\frac{1}{2}\beta + \frac{1}{2}c_0 f \quad (14)$$

(with  $c_0 = (15/2\pi)^{1/2}$ ) is the angular velocity of a deformed drop. Near the bifurcation point Eqs. (13) are accurate to  $O(\lambda^{-1})$  for  $\lambda \gg 1$ .

The angular velocity (14) involves drop rotation by the vorticity component of the flow (the first term on the right-hand side) and rotation by the straining component (the second term). The nonlinearity in the small-deformation equations (13) stems from the coupling between the drop rotation and the drop shape.

The terms proportional to the capillary number in Eqs. (13) describe drop relaxation, and the term  $\lambda^{-1}d$  corresponds to drop deformation by the external flow. The relaxation and deformation terms are  $O(\lambda^{-1})$ , whereas the rotation terms (the terms proportional to  $\omega_d$ ) are independent of the viscosity ratio.

All the terms in Eqs. (13) are necessary to describe the hysteretic drop behavior. Otherwise, the solutions do not capture the key features of the drop evolution.

### 2.3.3. Period doubling and chaotic dynamics

Numerical solutions of small-deformation equations for different values of flow parameters indicate that drop evolution undergoes a cascade of period-doubling bifurcations leading to chaos. A cascade of such bifurcations is depicted in Fig. 4, where we show the drop length at times  $t = nT$  ( $n = 1, 2, \dots$ ) vs. the amplitude of the vorticity oscillations for fixed values of the capillary number  $\text{Ca}$ , period  $T$  and mean vorticity  $\beta$ .<sup>1</sup>

Figures 4(a) and 4(b) correspond to two slightly different sets of parameters  $T$  and  $\beta$ . In both cases the first bifurcation occurs at  $\delta\beta \sim 0.065$ , and there is an inverse bifurcation cascade at large values of  $\delta\beta$ . The bifurcation diagram also shows windows of periodic motion (in particular, a large window in the range  $0.9 \lesssim \delta\beta \lesssim 0.12$  in Fig. 4(a)). We note that period doubling is found not only in our small deformation calculations but also in the boundary integral simulations of high-viscosity drops [4].

The time evolution of the drop deformation  $D$  and drop angle  $\phi$  near the first period-doubling bifurcation is depicted in Fig. 5. The bifurcation stems from the interplay between drop tumbling and vorticity oscillations. The key factor is the orientation of the drop when the vorticity parameter  $\beta(t)$  reaches a minimum. If the drop angle  $\phi$  does not exceed  $\pi/4$ , the drop rotation may be significantly slowed down or even reversed (owing to the straining flow component). On the other hand, for  $\phi > \pi/4$  the drop rotation is not hindered. Consequently, the period-doubling bifurcation leads to alternating accelerated and retarded drop-rotation cycles.

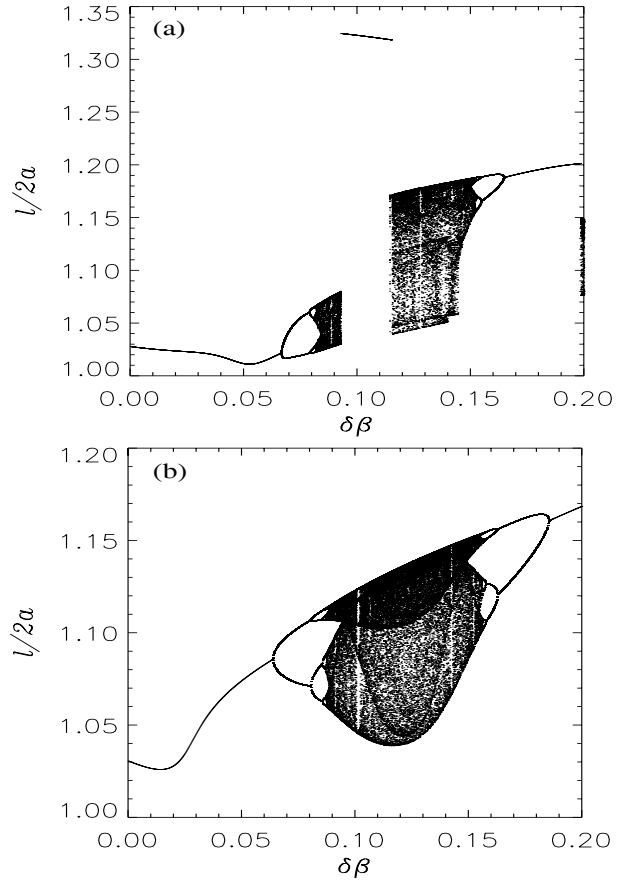


Figure 4: Bifurcation diagrams showing period doubling in flow with harmonic vorticity variation (11), for a drop with the viscosity ratio  $\lambda = 275$  and capillary number  $\text{Ca} = 0.2$ . Vorticity-variation parameters (a)  $\beta = 0.22$  and  $T/t_\sigma = 1.82$ , (b)  $\beta = 0.21$  and  $T/t_\sigma = 1.14$ . (Results from small-deformation theory).

### 2.3.4. Return map

To ascertain the chaotic nature of drop evolution, we perform an analysis of the return map for the small-deformation equations (13). The return map  $f_{n+1} = P(f_n)$  is constructed by plotting subsequent iterations  $f_{n+1}$  vs.  $f_n$  of the shape parameter  $f_n = f(nT)$ , at times equal to integer multiples  $n$  of the period  $T$ .

An example of the return map for specific values of the system parameters is shown in Fig. 6. All points of the map lie along a single curve—this behavior is consistent with the expectation that the period-doubling cascade leads to chaos on a low-dimensional attractor. The return map has one unstable fixed point at the intersection with the dashed line  $f_n = f_{n+1}$ .

To demonstrate that drop dynamics is chaotic for a given set of system parameters, we seek a period-three orbit of the map  $f_{n+1} = P(f_n)$ . The existence of such an orbit implies chaos [9]. A period-three orbit is obtained by analyzing the third iterate of the return map,  $f_{n+3} = P^3(f_n)$ . To calculate this iterate we first fit the return map  $f_{n+1} = P(f_n)$  with a polynomial (we used polynomials of order 20). The third iterate (a dash-dotted line

<sup>1</sup>For better accuracy the results shown in Fig. 4 were obtained using an expanded set of small deformation equations listed in [6, 4]; however, the asymp-

totic equations (13) yield similar results.

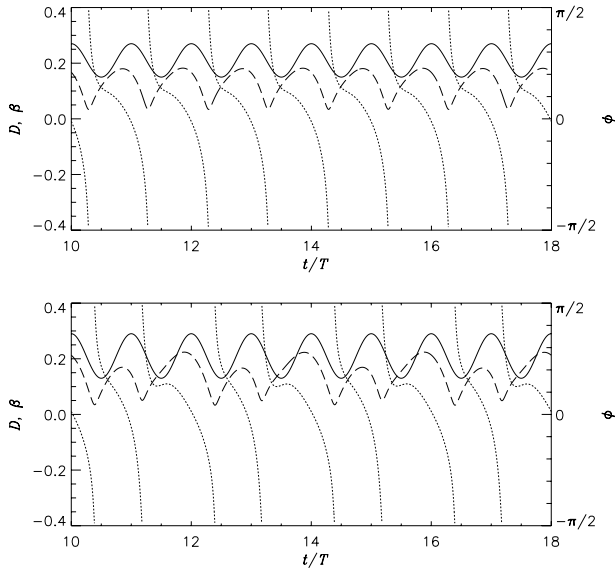


Figure 5: Illustration of the resonance that leads to period doubling. Vorticity parameter  $\beta$  (solid lines), drop deformation  $D$  (dashed), and drop angle  $\phi$  (dotted) are shown versus time  $t$  normalized by the oscillation period  $T$ . Viscosity ratio  $\lambda = 275$ , capillary number  $Ca = 0.2$ , period  $T/t_\sigma = 1.14$ , mean vorticity  $\bar{\beta} = 0.21$ , and vorticity oscillation amplitude (a)  $\delta\beta = 0.06$  and (b)  $0.08$ . (Results from small-deformation theory.)

in Fig. 6) is obtained by recursively applying this polynomial approximation.

The results presented in Fig. 6 indicate that the third iterate  $P^3(f_n)$  has six fixed points in addition to the period-one fixed point of the map  $P$ . These six fixed points (three stable and three unstable) correspond to two period-three orbits of the map  $P$ . Since the presence of period-three orbit implies chaos [9], we conclude that the drop evolution is chaotic.

The existence of chaos in the dynamical system (13) can also be demonstrated by showing that the stable and unstable manifolds (close to the unperturbed solution) intersect. To show the presence of such an intersection we have used the Melnikov integral. We have found that chaos exists as long as damping is small enough to prevent the solution from collapsing down to fixed points or simple periodic orbits. Moreover, chaos is not possible in the limit of very rapid forcing. These results will be presented in a forthcoming publication [10].

#### 2.4. Discussion

We have demonstrated that highly viscous drops in straining flow may undergo complex nonlinear evolution, which includes shape hysteresis, period-doubling bifurcations, and transition to chaos. To our knowledge the only other example of chaotic dynamics arising from interface instability in Stokes flow is the core-annular flow with insoluble surfactant adsorbed on the fluid interface [11].

We have shown that key features of drop dynamics can be described using a simple small-deformation theory that involves only two modes in the expansion of the drop shape into spherical harmonics. We note that similar techniques can be used to

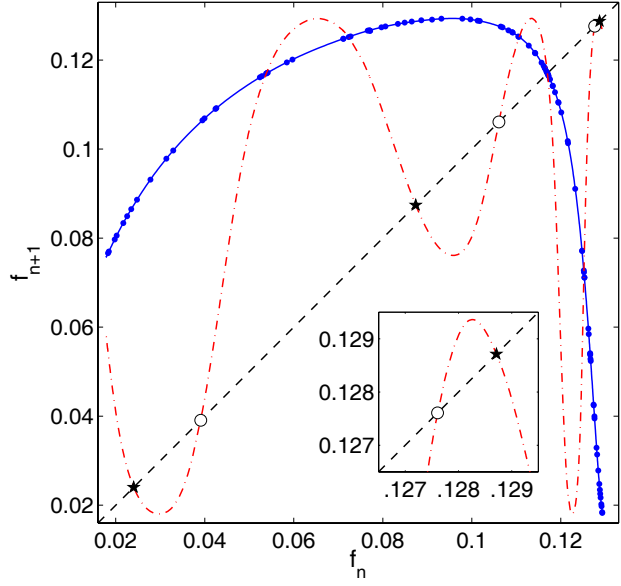


Figure 6: Return map (filled circles) for the shape parameter  $f$  with  $\lambda = 276$ ,  $Ca = 0.2$ ,  $\beta = 0.21$ ,  $\delta\beta = 0.062$ , and  $T/t_\sigma = 1.45$ . Solid line is a polynomial fit to the return map, dash-dotted line is the third-iterate map, and the dashed line is  $f_{n+1} = f_n$ . Two additional sets of fixed points of the third-iterate map correspond to the two orbits with period three: open circles are the three stable fixed points and stars are the three unstable fixed points. The inset shows the closeup of the two fixed points on the right.

study evolution of other deformable particles, such as vesicles [12, 13] or macromolecules [14].

Our results can also be applied to evaluate rheological response of dilute dispersions in which particles deform, but interparticle hydrodynamic interactions can be neglected. In Sec. 3 we analyze a different set of problems: we focus on the role of interparticle hydrodynamic interactions in systems where particles are nondeformable.

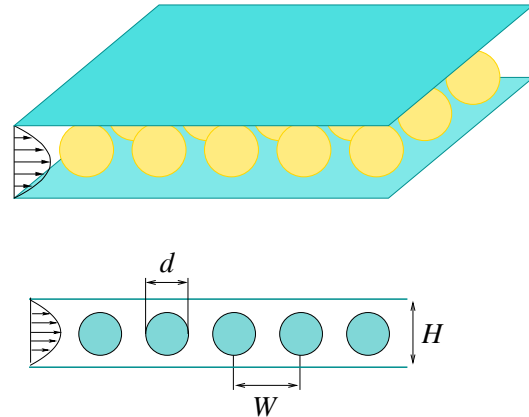


Figure 7: System geometry: particle array in a parallel-wall channel.

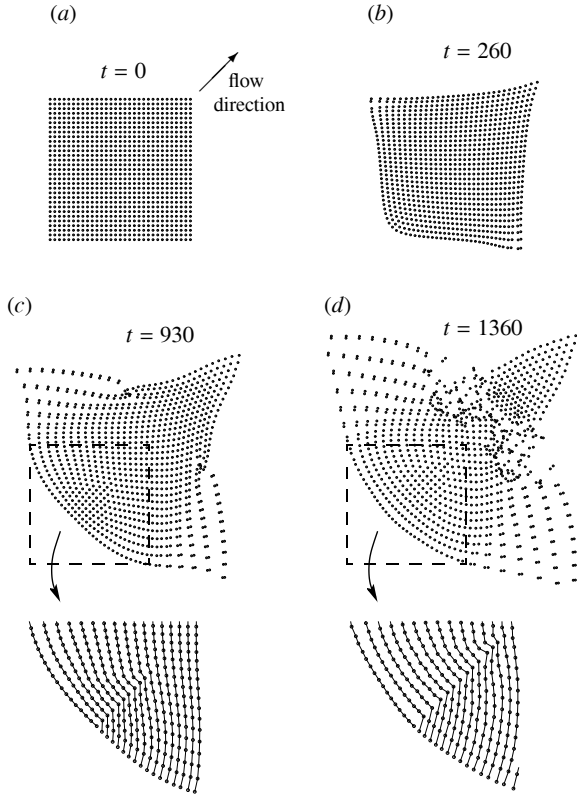


Figure 8: Evolution of initially square array of  $N = 961$  particles in Poiseuille flow in a parallel-wall channel of width  $H/d = 1.1$ . Interparticle spacing  $W/d = 5$ . The time  $t$  is scaled by the time an isolated particle in the channel travels the distance equal to its diameter  $d$ . The insets show development of the dislocation line in the region marked by the square.

### 3. Collective dynamics of particle arrays in a parallel-wall channel

Our second example of nonlinear evolution in two-phase systems under Stokes-flow conditions is the behavior of arrays of rigid spherical particles freely suspended in a fluid. The arrays are driven either by an external flow or force. Since the particles are nondeformable, the nonlinear dynamics stems from the interparticle hydrodynamic interactions.

We focus on collective dynamics induced by confinement in parallel-wall channels. Recent investigations have revealed that confining walls significantly affect particle evolution, leading to phenomena that do not occur in free space [15, 16, 17, 5]. These phenomena include enhanced relative particle diffusivity due to a backflow effect [15, 18], amplified transverse hydrodynamic resistance of long particle chains [19, 18, 20, 21], wave propagation in linear particle arrays in Poiseuille flow, [16, 17, 5], and structural transitions in flow-driven 2D particle arrays [5].

#### 3.1. Dynamics of ordered flow-driven particle arrays

Collective evolution of regular quasi-2D arrays of neutrally buoyant spherical particles is examined in a parallel-wall channel under strong-confinement conditions  $H/d \lesssim 2$  (where  $H$  is the channel width and  $d$  is the particle diameter). The particle

arrays are driven by Poiseuille flow produced by a constant applied pressure gradient. The geometry of the system is depicted in Fig. 7.

Examples of collective phenomena observed in flow-driven arrays with initial square ordering are illustrated in Figs. 8 and 9. The results were obtained using our highly accurate accelerated Stokesian-dynamics algorithm [19, 5, 22]. Figure 8 shows the evolution of a finite initially square array of  $N \approx 10^3$  particles driven in the diagonal direction. An infinite periodic array driven in the lateral direction is depicted in Fig. 9. The array in Fig. 8 is in the midplane of the channel  $z = H/2$  (where  $z$  is the distance from the lower wall) and the array in Fig. 9 is in the off-center plane  $z \approx H/3$ , with some scatter of vertical particle positions  $z$ .

The finite-size array in Fig. 8 undergoes macroscopic deformation accompanied by a sequence of structural transitions. Initially, the particles maintain their original ordering on the deformed square lattice. Next, double rows of particles separate from the array, forming a shape similar to airplane wings. As the evolution progresses, an instability occurs at the junction between the wings and the body of the array; from the instability point there spreads a region of disordered particle motion. Moreover, the simulations also show that at the rear end of the array the particle lattice undergoes a discontinuous rearrangement along a fault line that develops at the axis of symmetry. As depicted in the blowups of the dislocation region, the particles realign into a new square lattice, with a different (i.e. diagonal) orientation.

Intriguing topological transitions also occur in infinite arrays. In the initial frame shown in Fig. 9(a) there is a density wave in the rectangular lattice. This longitudinal density wave propagates in the flow direction, but it also dissipates. At time  $T = 700$  the wave has nearly dissipated, and the vertical particle scatter (not shown) has significantly decreased. At this point, the array undergoes a sudden transition to a polycrystalline hexagonal lattice. The fact that this transition has not occurred earlier indicates that the array was stabilized by random particle displacements. The lattice subsequently evolves into a state with string-like particle arrangements but no long-range order. At much later times particles form clusters.

The complex collective dynamics illustrated in Figs. 8 and 9 is of purely hydrodynamic origin—there are no direct interparticle forces in our system. Hydrodynamic interactions are thus responsible for macroscopic deformation of the arrays, wave propagation, tendency of the system to maintain ordered structure, and for the array instabilities. Detailed mechanisms responsible for this complex behavior are not known. However, our effective-medium theory, discussed in Sec. 3.2 can provide an insight.

#### 3.2. Effective-medium approach

The macroscopic evolution of the array shape can be described using a simple quasi-2D effective-medium approximation. In this approach [5, 22], the suspension dynamics is described in terms of the average suspension velocity  $\mathbf{u}$  and macroscopic particle flux  $\mathbf{j}_p$ , which satisfy the 2D continuity

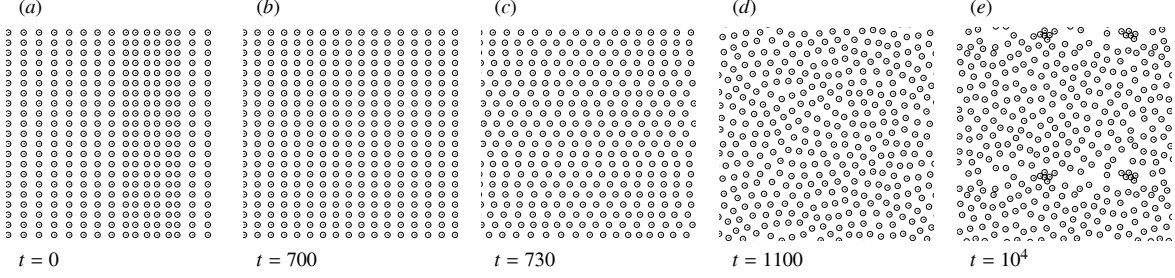


Figure 9: Evolution of infinite quasi-two-dimensional particle array in a parallel-wall channel of width  $H/d = 1.9$ . Particles are distributed, with some scatter, near the plane  $z = 0.7d$  (where  $z = 0$  is the position of the lower wall). (a) Initial configuration with a propagating longitudinal displacement wave; (b) the displacement wave and vertical fluctuations have dispersed; (c) transition to a polycrystalline state with hexagonal order suddenly occurs; (d) string-like particle order develops; (e) particle clusters begin to form.

equations

$$\nabla_{\parallel} \cdot \mathbf{u} = 0, \quad \frac{\partial n_s}{\partial t} = -\nabla_{\parallel} \cdot \mathbf{j}_p. \quad (15)$$

Here  $\nabla_{\parallel}$  denotes lateral gradient operator,  $t$  is time, and  $n_s$  is the particle density per unit area. The lateral fluxes  $\mathbf{u}$  and  $\mathbf{j}_p$  are linked to the local macroscopic pressure gradient  $\nabla_{\parallel} \bar{p}$  via the linear constitutive relations

$$\mathbf{u} = -\kappa \nabla_{\parallel} \bar{p}, \quad \mathbf{j}_p = -n_s \nu \nabla_{\parallel} \bar{p}, \quad (16)$$

where the transport coefficients  $\kappa$  and  $\nu$  (i.e., the channel permeability and collective mobility) depend on  $n_s$ .

We have solved Eqs. (15) and (16) in the weak-coupling regime, where the channel permeability  $\kappa = \kappa_0 + \delta\kappa$  only slightly differs from the permeability  $\kappa_0$  of a particle-free channel, and the collective mobility coefficient  $\nu$  equals the mobility of an isolated particle in the channel. In this regime, the particle contribution  $\nabla_{\parallel} \delta \bar{p}$  to the macroscopic pressure gradient

$$\nabla_{\parallel} \bar{p} = \nabla_{\parallel} p^{\text{ext}} + \nabla_{\parallel} \delta \bar{p} \quad (17)$$

(where  $\nabla_{\parallel} p^{\text{ext}}$  is the applied pressure gradient) can be obtained from the superposition of 2D dipolar far-field pressure contributions

$$p_1(\boldsymbol{\rho} - \boldsymbol{\rho}') = -\mathbf{D}_0 \cdot \nabla_{\parallel} \log(|\boldsymbol{\rho} - \boldsymbol{\rho}'|) \quad (18)$$

resulting from interaction of the external flow with individual particles [20, 22]. Here  $\boldsymbol{\rho}$  and  $\boldsymbol{\rho}'$  denote the lateral positions of the field point and particle center, respectively. The particle dipole moment  $\mathbf{D}_0$ , which depends on the channel width and the position of the array with respect to the channel walls, is independent of the particle position in the array. Assuming constant particle density  $n_s$  in the array and using the Gauss formula, the particle contribution to the local pressure gradient can be expressed as a line integral

$$\nabla_{\parallel} p \delta(\boldsymbol{\rho}) = n_s \mathbf{D}_0 \cdot \int_{C'} \hat{\mathbf{n}}' \nabla_{\parallel} \log(|\boldsymbol{\rho} - \boldsymbol{\rho}'|) dl' \quad (19)$$

over the contour  $C'$  representing the boundary of the array (where  $\hat{\mathbf{n}}'$  denotes the outward vector normal to the contour  $C'$ , and the integration is over the primed variables).

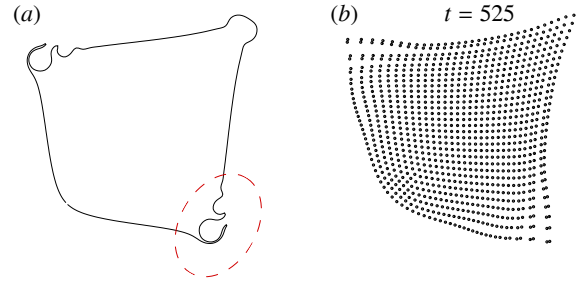


Figure 10: Evolution of initially square particle array in diagonal motion. (a) Results of effective-medium theory; (b) simulation results for the same system as the one depicted in Fig. 8. The two frames (a) and (b) correspond to the same stage of evolution. The effective-medium theory predicts fingering instability in the region indicated by the ellipse, but for the system shown in (b) this instability is suppressed.

We have used relations (16) and (19) to calculate the evolution of an initially square array with rounded corners (smoothing of the initial condition is needed to avoid a singular behavior). In Fig. 10 our calculations are compared with the direct simulations depicted in Fig. 8. The comparison shows that our theory reproduces quite well the evolution of the overall array shape, until complex structural features develop.

The theory also predicts a fingering instability near the array corners (in the region indicated in Fig. 10(a) by the ellipse). In the array depicted in Figs. 8 and 10(b) this instability is suppressed due to the tendency of the particles to maintain their order. Such an instability occurs, however, for a smaller inter-particle distance  $W/d = 2$  (cf. Fig. 11).

The effective-medium theory is successful in describing the effect of the flow scattered by the array particles on the overall array motion. However, this model is insufficient for a description of fine structural features in the array. A discussion how the validity range of the effective-medium theory can be extended is presented at the end of Sec. 3.3.

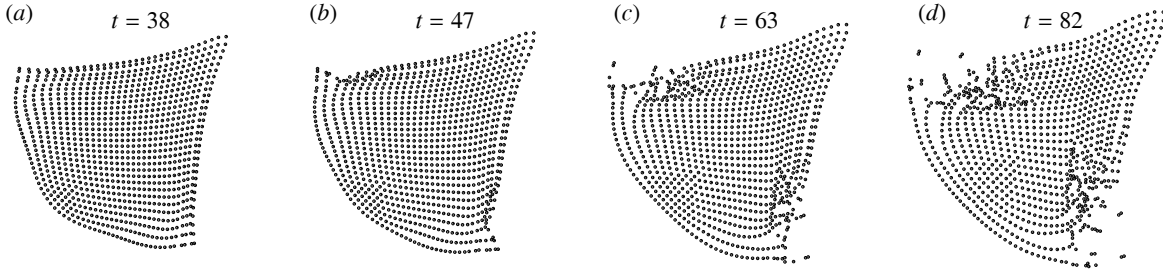


Figure 11: Development of fingering instability in a flow-driven square array with initial interparticle spacing  $W/d = 2$ . The remaining system parameters are the same as in Fig. 8.

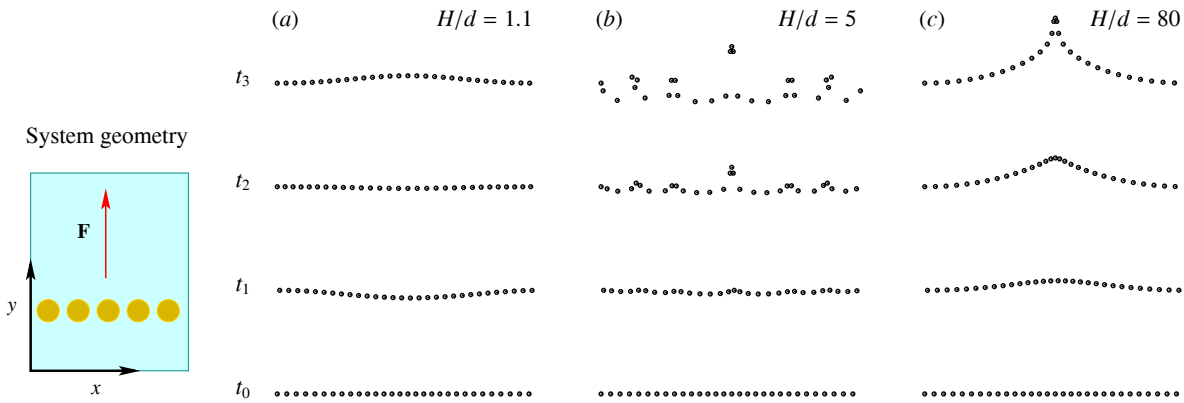


Figure 12: Evolution of a force-driven infinite linear particle array with average interparticle spacing  $W/d = 3$ . The array is in the midplane of the channel, and equal driving force  $F$  (parallel to the walls and normal to the array) is applied to all particles. At the initial time  $t_0$  there is a small-amplitude density wave of length  $\lambda = 30W$  in the array.

### 3.3. Stability of confined particle arrays

Collective phenomena discussed in Sec. 3.1 and 3.2 were observed for strongly confined particle arrays (i.e., for channel widths comparable to the particle diameter). The effect of the wall separation on the array evolution has not been determined yet. To illustrate some key differences in the behavior of strongly and weakly confined arrays, we analyze the evolution of an infinite linear particle chain in channels with different normalized width  $H/d$ .

We assume that the chain is parallel to the axis  $x$ , moves in the midplane of the channel, and is driven by the constant force  $\mathbf{F} = F\hat{\mathbf{e}}_y$  (normal to the chain and parallel to the walls), applied to all particles. In Fig. 12 we show evolution of a chain in channels with three different wall separations. In the initial configuration at  $t = t_0$  the chain is slightly perturbed from a uniform configuration. The perturbation corresponds to a small-amplitude density wave of length  $\lambda = 30W$ , with the maximum at the center of the depicted portion of the chain. A strongly confined chain (with  $H/d = 1.1$ ) is stable (cf. Fig. 12(a)). In contrast, the moderately and weakly confined chains represented in Figs. 12(b) and 12(c) are unstable.

The stability of strongly confined chains and instability of weakly confined ones can be explained using a simple continuum model. In this model it is assumed that hydrodynamic

interactions between distant parts of a chain can be neglected. Thus in the long-wave limit, the local velocity of a deformed chain can be expressed by the mobility relation

$$\mathbf{v}(s) = \boldsymbol{\mu}(s) \cdot \mathbf{F}, \quad (20)$$

where  $s$  is the position along the chain. The local mobility  $\boldsymbol{\mu}(s)$  depends on the local values of the chain orientation  $\alpha(s)$  and particle density per unit length  $n_1(s)$ . This dependence is given by the relation

$$\boldsymbol{\mu}(s) = \boldsymbol{\mu}_0(n_1(s), \alpha(s)), \quad (21)$$

where  $\boldsymbol{\mu}_0(n_1, \alpha)$  is the mobility of an infinite undeformed chain of density  $n_1$  and orientation  $\alpha$ .<sup>2</sup>

By symmetry, the mobility tensor  $\boldsymbol{\mu}_0$  can be split into the normal and tangential components

$$\boldsymbol{\mu}_0 = \mu_{\perp} \hat{\mathbf{n}}\hat{\mathbf{n}} + \mu_{\parallel} \hat{\mathbf{t}}\hat{\mathbf{t}}, \quad (22)$$

<sup>2</sup>The flow field produced by a point force in a channel decays as  $\rho^{-2}$  for lateral distances  $\rho \gg H$ . Therefore, relations (20) and (21) are exact in the asymptotic regime  $\lambda \gg H$  (where  $\lambda$  is the characteristic distance for variation of the chain density and shape). In the intermediate regime  $d < \lambda < H$  the long range  $O(\rho^{-1})$  contributions from regions  $\lambda \lesssim \rho \lesssim H$  cannot be neglected, and thus, in this range, our model captures key features of the system dynamics qualitatively but not quantitatively.

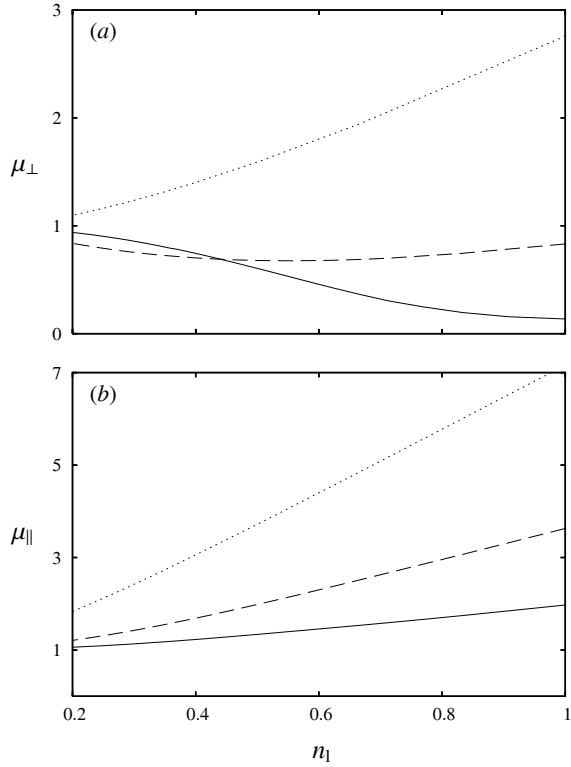


Figure 13: (a) Transverse and (b) lateral mobility of infinite linear chain of spherical particles in a parallel-wall channel of width  $H/d = 1.1$  (solid line),  $H/d = 5$  (dashed), and  $H/d = 80$  (dotted) vs. chain density  $n_1 = d/W$ . The results are normalized by the corresponding results in the low-density limit.

where  $\hat{n}$  is the local normal unit vector and  $\hat{t}$  unit vector tangent to the chain. The dependence of the transverse and longitudinal mobility coefficients  $\mu_{\perp}$  and  $\mu_{\parallel}$  on the chain density, for several values of wall separation  $H$ , is illustrated in Fig. 13. The main features to be noted are

$$\mu_{\parallel} > \mu_{\perp} \quad (23)$$

and

$$d\mu_{\perp}/dn_1 < 0, \quad \text{for } H \approx d, \quad (24a)$$

$$d\mu_{\perp}/dn_1 > 0, \quad \text{for } H \gg d. \quad (24b)$$

The different signs of the derivatives (24) for strongly confined and weakly confined chains stem from the backflow effect discussed in [18, 19, 20]. Namely, since there is no net flow in the channel, fluid in a tightly-confined system has to squeeze through the gaps between the wall and the moving chain or through the spaces between the chain particles. Hence, the transverse mobility decreases with increasing particle density. In contrast, for weakly confined systems, dense chains move faster, because of the larger force per unit length of the chain.

Inequalities (23) and (24) have important consequences for stability of the chain in transverse motion. This can be seen by

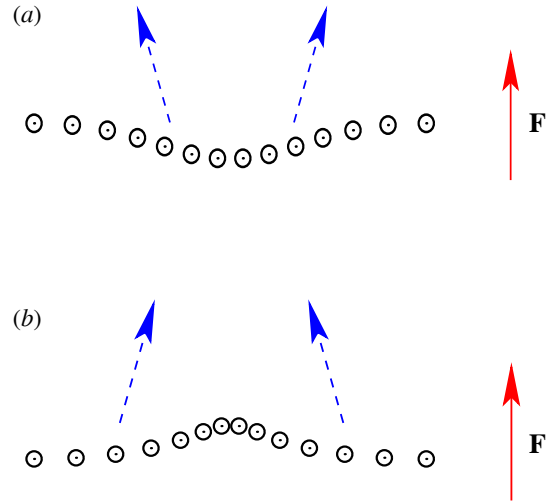


Figure 14: Dynamics of (a) strongly confined and (b) weakly confined particle chain in transverse motion. In the strongly confined chain the dense region stays behind, which causes relaxation of the density perturbation because adjacent portions of the chain slide outwards. In the weakly confined chain the dense region moves faster, which causes growth of the density perturbation because the adjacent portions of the chain move inwards.

considering a small perturbation

$$n_1(x, t) = n_0 + \delta n_1(x, t), \quad y(x, t) = y_0(t) + \delta y(x, t), \quad (25)$$

of the chain density and shape from a uniform state with constant density  $n_0$ . The particles are positioned on the horizontal line  $y_0 = v_0 t$  moving with the chain velocity  $v_0 = \mu_{\perp}(n_0)F$ . Using relations (20)–(22) and (25) we find the evolution equations for the perturbations of the chain density and shape

$$\frac{\partial}{\partial t} \delta n_1 = -(\mu_{\parallel} - \mu_{\perp}) \frac{\partial^2}{\partial x^2} \delta y, \quad (26a)$$

$$\frac{\partial}{\partial t} \delta y = \frac{d\mu_{\perp}}{dn_1} \delta n_1. \quad (26b)$$

Assuming a solution in the form of Fourier modes

$$\delta n_1 = A e^{i(kx - \omega t)}, \quad \delta y = B e^{i(kx - \omega t)}, \quad (27)$$

we obtain the dispersion relation

$$\omega = \pm \left[ -(\mu_{\parallel} - \mu_{\perp}) \frac{d\mu_{\perp}}{dn_1} \right]^{1/2} k. \quad (28)$$

The inequalities (23) and (24) thus imply that the frequency  $\omega$  is real for strongly confined systems with  $H \approx d$  and  $\omega$  is imaginary for weakly confined systems with  $H \gg d$ . In the former case the system is stable, with coupled longitudinal and transverse waves. In the latter case the system is unstable, and initial perturbations grow exponentially. The mechanism leading to the different behavior of weakly and strongly confined chains is illustrated in Fig. 14.

The chain evolution depicted in Fig. 12 is consistent with the above analysis. For  $H/d = 1.1$  we observe standing-wave oscillations of coupled longitudinal and transverse modes (cf. Fig. 12(a)). For  $H/d = 80$  Fig. 12(c) shows an instability due to the exponential growth of the initial long-wave perturbation. For  $H/d = 5$  the long-wave modes are stable, but the system decomposes via unstable short-wave modes (cf. Fig. 12(b)).

The analysis presented above can be generalized to 2D arrays. To determine the effect of the deformation of particle lattice on the array motion, the scalar transport coefficients  $\kappa$  and  $\nu$  in the effective-medium equations (16) should be replaced with tensorial coefficients  $\boldsymbol{\kappa}$  and  $\boldsymbol{\nu}$  that depend on the local lattice vectors. We expect that such a modified effective medium theory will explain why the fingering instability occurs only in sufficiently dense suspensions. It is also tempting to speculate that the fault line that develops in the rear end of the array (shown in Fig. 8) can be described as a shock in the solution.

### 3.4. Discussion

Our Stokesian dynamics simulations revealed that strongly confined regular particle arrays in Poiseuille flow undergo complex structural evolution. We have observed discontinuous re-orientation of particle lattice, stabilization of quasi-2D ordered systems by random particle displacements, and order-disorder transitions.

Some aspects of the system dynamics, such as the evolution of the array shape and a fingering instability have been described using an effective medium theory. A simple continuum model has also been used to elucidate differences in stability of confined and unconfined particle arrays.

Our present results are numerical and theoretical. It would be interesting to perform experiments in which ordered particle arrays are assembled using holographic optical tweezers [23].

## 4. Conclusions

We have analyzed nonlinear hydrodynamic phenomena that occur in creeping flows of two-phase dispersions. Two important classes of nonlinear behavior have been considered: the dynamics of individual deformable drops in external flows, and the motion of assemblies of hydrodynamically coupled rigid particles. In the first case the nonlinear evolution results from the coupling between the fluid flow and the drop shape. In the second case the nonlinear dynamics is a consequence of multi-particle hydrodynamic interactions.

For both systems we have found complex nonlinear evolution: bistability and chaotic dynamics for individual drops; and wave propagation, lattice rearrangements, and fingering instabilities in flow-driven regular particle arrays. Moreover, our additional simulations have revealed complex irregular evolution of coupled harmonic waves in flow-driven particle chains—in our future investigations we will determine if this irregular evolution is chaotic.

We have given separate descriptions of particle deformation and interparticle hydrodynamic interactions because of the complexity of these nonlinear phenomena. In many physical

problems, however, the effects described in our paper need to be considered together. For example, in studies of emulsion flows [24, 25, 26] and blood circulation [27] particle deformation and interparticle hydrodynamic interactions are coupled.

The techniques used here to analyze the behavior of individual drops and the motion of particle arrays can be combined to describe the evolution of suspensions of soft particles. We have recently shown that the dynamics of chains of deformable drops in parallel wall channels can be described in this way [28].

Finally, macromolecular solutions can also be studied using our methods. For example, the approach that we have applied to analyze bistable dynamics of viscous drops can be successfully employed to describe the evolution of DNA macromolecules in linear flows [14]. Our results can thus shed light on numerous aspects of nonlinear dynamics of complex fluids.

## Acknowledgements

JB was supported by NSF CAREER Grant No. CBET-0348175. YNY acknowledges a NSF/DMS grant (DMS-0708977) and a SBR grant from NJIT. RG was supported by a NSF/DMS grant (DMS-0506495). The simulations were conducted on the NJIT computer cluster supported by NSF/MRI grant DMS-0420590.

## References

- [1] S. Chandrasekhar, Hydrodynamic and Hydromagnetic Stability, Clarendon, 1961.
- [2] M. C. Cross, P. C. Hohenberg, Pattern-formation outside of equilibrium, Rev. Mod. Phys. 65 (1993) 851–1112.
- [3] I. Procaccia, K. R. Sreenivasan, The state of the art in hydrodynamic turbulence: Past successes and future challenges, Physica D 237 (2008) 2167–2183.
- [4] Y.-N. Young, J. Bławdziewicz, V. Cristini, R. H. Goodman, Hysteretic and chaotic dynamics of viscous drops in creeping flows with rotation, J. Fluid Mech. 607 (2008) 209–234.
- [5] M. Baron, J. Bławdziewicz, E. Wajnryb, Hydrodynamic crystals: collective dynamics of regular arrays of spherical particles in a parallel-wall channel, Phys. Rev. Lett. 100 (2008) 174502.
- [6] J. Bławdziewicz, V. Cristini, M. Loewenberg, Multiple stationary states for deformable drops in linear Stokes flows, Phys. Fluids 15 (2003) L37–40.
- [7] V. Cristini, J. Bławdziewicz, M. Loewenberg, An adaptive mesh algorithm for evolving surfaces: Simulations of drop breakup and coalescence, J. Comput. Phys. 168 (2001) 445–463.
- [8] P. Vlahovska, J. Bławdziewicz, M. Loewenberg, Deformation of a surfactant-covered drop in a linear flow, Phys. Fluids 17 (2005) 103103–1–18.
- [9] T. Li, J. A. Yorke, Period three implies chaos, Amer. Math. Monthly 82 (1975) 985–992.
- [10] R. Goodman, Y.-N. Young, J. Bławdziewicz, On the chaotic nature of viscous drop dynamics in Stokes flow, Phys. Rev. E in preparation.
- [11] S. Kas-Danouche, D. T. Papageorgiou, M. Siegel, Nonlinear dynamics of core-annular film flows in the presence of surfactant, J. Fluid Mech. submitted.
- [12] C. Misbah, Vacillating breathing and tumbling of vesicles under shear flow, Phys. Rev. Lett. 96 (2006) 028104.
- [13] P. M. Vlahovska, R. S. Gracia, Dynamics of a viscous vesicle in linear flows, Phys. Rev. E 75 (2007) 016313.
- [14] J. Bławdziewicz, Macromolecules and deformable drops in linear flows with vorticity: a second conformation transition, Bul. Am. Phys. Soc. 51 (2006) Abstract KB.00001.

- [15] B. Cui, H. Diamant, B. Lin, S. A. Rice, Anomalous hydrodynamic interaction in a quasi-two-dimensional suspension, *Phys. Rev. Lett.* 92 (2004) 258301–1–4.
- [16] T. Beatus, T. Tlusty, R. Bar-Ziv, Phonons in a one-dimensional microfluidic crystal, *Nature Phys.* 2 (2006) 743–748.
- [17] T. Beatus, T. Tlusty, R. Bar-Ziv, Anomalous microfluidic phonons induced by the interplay of hydrodynamic screening and incompressibility, *Phys. Rev. Lett.* 99 (2007) 124502.
- [18] S. Bhattacharya, J. Bławdziewicz, E. Wajnryb, Hydrodynamic interactions of spherical particles in suspensions confined between two planar walls, *J. Fluid Mech.* 541 (2005) 263–292.
- [19] S. Bhattacharya, J. Bławdziewicz, E. Wajnryb, Many-particle hydrodynamic interactions in parallel-wall geometry: Cartesian-representation method, *Physica A* 356 (2005) 294–340.
- [20] S. Bhattacharya, J. Bławdziewicz, E. Wajnryb, Hydrodynamic interactions of spherical particles in Poiseuille flow between two parallel walls, *Phys. Fluids* 18 (2006) 053301.
- [21] Y. Han, A. Alsayed, M. Nobili, J. Zhang, T. C. Lubensky, A. G. Yodh, Brownian Motion of an ellipsoid, *Science* 314 (2006) 626–630.
- [22] J. Bławdziewicz, E. Wajnryb, An analysis of the far-field response to external forcing of a suspension in Stokes flow in a parallel-wall channel, *Phys. Fluids*. 20 (2008) 093303.
- [23] S. C. Chapin, V. Germain, E. R. Dufresne, Automated trapping, assembly, and sorting with holographic optical tweezers, *Opt. Express* 14 (2006) 13095–13100.
- [24] T. Thorsen, R. W. Roberts, F. H. Arnold, S. R. Quake, Dynamic pattern formation in a vesicle-generating microfluidic device, *Phys. Rev. Lett.* 86 (2001) 4163–4166.
- [25] A. Vananroye, P. Van Puyvelde, P. Moldenaers, Structure development in confined polymer blends: Steady-state shear flow and relaxation, *Langmuir* 22 (2006) 2273–2280.
- [26] J.-R. Huang, T. G. Mason, Shear oscillation light scattering of droplet deformation and reconfiguration in concentrated emulsions, *Europhys. Lett.* 83 (2008) 28004.
- [27] J. B. Freund, Leukocyte margination in a model microvessel, *Phys. Fluids* 19 (2007) 023301.
- [28] P. J. A. Janssen, M. D. Baron, J. Bławdziewicz, M. Loewenberg, P. D. Anderson, A simplified description for the collective dynamics of linear arrays of drops in parallel-wall microchannels, *AIChE Annual Meeting, Philadelphia*, 16–21 November 2008 (2008).